Applied Clay Science 276 (2025) 107911

Contents lists available at ScienceDirect

Applied Clay Science

journal homepage: www.elsevier.com/locate/clay

Research Paper

Self-sealing capacity of boom clay affected by an alkaline plume: Evidences from high resolution X-ray computed tomography and hydraulic conductivity measurements☆

Miroslav Honty [a,*], Lander Frederickx [a], Ivan Josipović [b], Matthieu N. Boone [b], Pascale Senechal [c], Stéphane Faucher [c], Séverine Levasseur [d], Xavier Sillen [d]

[a] SCK-CEN, Belgian Nuclear Research Centre, Mol, Belgium
[b] UGCT – Department of Physics and Astronomy, Gent University, Belgium
[c] Université de Pau et des Pays de l'Adour, CNRS, DMEX, Pau, France
[d] ONDRAF/NIRAS, Belgian National Agency for Radioactive Waste and Enriched Fissile Materials, Brussels, Belgium

ARTICLE INFO

Keywords:
Boom Clay
Geological disposal
Self-sealing capacity
Alkaline plume
micro-CT

ABSTRACT

This study aims to evaluate the self-sealing capacity of the Boom Clay when perturbed by an alkaline plume, by investigating the long-term evolution of hydraulic conductivity and mineralogical changes in fractured Boom Clay upon interaction with highly alkaline solutions. In a first step, percolation experiments were conducted on undisturbed clay samples using Young Cement Water (YCW, pH of 13.5) and Evolved Cement Water (ECW, pH of 12.6), both parallel and perpendicular to bedding planes. Hydraulic conductivity (K) in these alkaline environments were estimated, confirming the previous studies, with higher horizontal than vertical hydraulic conductivity as a result of the natural anisotropy of the Boom Clay. In a second step, clay samples were fractured. All samples experienced a significant increase in K, followed by a progressive decrease, indicative of an efficient self-sealing. This self-sealing process was visualized using X-ray micro computed tomography and spectral micro computed tomography analysis.

In addition, mineralogical analyses, including specific surface area and pore size distributions from N_2-physisorption, (Quantitative) X-ray diffraction and Fourier Transform Infrared spectroscopy analysis were conducted. They revealed partial dissolution of smectite in YCW environments but no significant mineral alteration in ECW-percolated samples. N_2-physisorption experiments of the post-mortem samples indicated decrease of the specific surface area and concomitant decrease in the microporosity in all studied cases. Though the decrease in the specific surface area and microporosity can be explained by partial dissolution of smectite in the YCW environment, the shift of the pore size distribution towards larger pores can be linked to relative density changes in the vicinity of the fractures and overall increase in hydraulic conductivity. The results confirmed that Boom Clay retains its self-sealing capacity, even after prolonged exposure to high-pH conditions. This study provides valuable insights into the hydro-mechanical and mineralogical response of Boom Clay, essential for assessing its long-term behaviour as a geological barrier.

1. Introduction

Self-sealing is an important property of clay formations studied as caprocks for the long-term CO_2 storage (Hou et al., 2022; Tian et al., 2014) or as natural barriers for the long-term geological disposal of radioactive waste (Bock, 2014). In the context of the geological disposal, the fractures in the host formations are formed during the construction of the repository as a result of the excavation of the shafts and the galleries, leading to a so-called Excavation Damaged Zone (EDZ) around these structures (Bernier et al., 2007; Van Marcke and Bastiaens, 2010). The fractures may serve as preferential pathways for radionuclide migration in the natural barrier. Therefore, the self-sealing capacity of the clay formations is an important item to consider in the assessment of the functioning of a geological repository.

☆ This article is part of a Special issue entitled: 'Clay Conf. Hannover 2024' published in Applied Clay Science.

* Corresponding author.
E-mail address: mhonty@sckcen.be (M. Honty).

https://doi.org/10.1016/j.clay.2025.107911
Received 19 March 2025; Received in revised form 10 June 2025; Accepted 11 June 2025
Available online 17 June 2025

Self-sealing is understood as a reduction of fracture permeability by any natural, i.e. spontaneous hydromechanical, hydrochemical, or hydrobiochemical process (Bastiaens et al., 2007). Self-sealing has to be distinguished from self-healing which is defined as sealing with loss of memory of the pre-sealing state. It means that a healed fracture will have the same hydromechanical properties than an intact clay, whereas a sealed fracture will only recover the hydraulic properties of the intact clay. Though the importance of the specific mechanism in the self-sealing phenomenon is still matter of debate, it is generally accepted that clay swelling, the consolidation/re-compaction and the creep jointly play a role in the self-sealing process (Gonzalez-Blanco et al., 2024).

The Boom Clay, Callovo-Oxfordian Clay and Opalinus Clay are studied either as potential candidate or selected natural barriers for geological disposal of radioactive waste in Belgium, France and Switzerland respectively. The self-sealing capacity of these clay formations have been demonstrated by numerous in-situ and laboratory tests (e.g., Bossart et al., 2004; Chen et al., 2014; Di Donna et al., 2022; Van Geet et al., 2008; Van Marcke and Bastiaens, 2010; Wang et al., 2024; Zhang, 2011; Zhang and Talandier, 2023). In these studies, the natural or synthetic pore waters mimicking in-situ conditions were used for water saturation and permeability tests. It means that the self-sealing capacity of these clays were only studied in geochemical equilibrium imposed by the natural conditions (i.e., with limited chemical impacts due to low chemical gradients between solids and pore waters).

The current geological disposal concepts involve pervasive use of concrete and cementitious materials as part of engineered barrier systems (e.g., Ma et al., 2024; Wilson et al., 2021). The release of aggressive highly alkaline fluids is expected during operational and post-closure phase of the repository as a result of concrete degradation. The fluids emanating from cement at early stages of hydration will be dominated by dissolution of Na/K hydroxides (Berner, 1992) leading to a pH of 13.0–13.5. In this study, the effects of these waters, denoted YCW (Young Cement Water) are studied on Boom Clay. In the later stage of the concrete degradation, the chemical composition of the pore fluid will be controlled by the solubility of portlandite – $Ca(OH)_2$ (Atkinson et al., 1989), buffering the pH at 12.5. The effects of these waters on Boom Clay are also studied in this article and denoted hereafter ECW (Evolved Cement Water). Clearly, these waters have different chemical composition and pH compared to formation waters. Consequently, they will react with the minerals present in the clay host formations, potentially trigger mineral dissolution and precipitation reactions. To properly evaluate the functioning of a geological disposal that includes components made of concrete, it is necessary to evaluate if clay, in contact with cementitious materials over a long period of time, retains its self-sealing capacity. Extensive research has been devoted to studying the interaction between hyperalkaline solutions and compacted bentonites, (e.g., Dolder et al., 2014; Fernández et al., 2010; Fernández et al., 2009; Nakayama et al., 2004) as well as between concrete and natural barriers (Bernard et al., 2023; Gaboreau et al., 2011; Techer et al., 2012). A common mineralogical feature observed in these studies is the dissolution of smectite, accompanied by the precipitation of secondary minerals, like C(*A*)SH, calcite or zeolite. These processes may lead to both porosity increase or decrease (Lalan et al., 2019; Mäder et al., 2017) depending on the location of the reaction front and experimental conditions. In this study, a different approach was taken. Boom Clay cores were first percolated with highly alkaline solutions, then artificially fractured, and subsequently percolated again with the same solutions. The aim was to investigate whether the host rock retains its self-sealing capacity after reacting with highly alkaline solutions, as the self-sealing behaviour of potential host rocks is well documented under natural conditions (see above).

It is important to note that the effect of the alkaline plume on the Boom Clay was previously addressed by (Wang et al., 2010). After approximately 15 years of percolation, hydraulic conductivity increased by a factor of two in the YCW environment and decreased by about 20 % in the ECW. The increase in permeability was attributed to the dissolution of smectite and organic matter in the YCW, while the decrease in the ECW was tentatively linked to porosity occlusion due to calcite precipitation, as predicted by geochemical modelling. Although smectite and organic matter dissolution was confirmed experimentally, no precipitation of secondary phases could be detected by either X-ray diffraction analysis or scanning electron microscopy. Moreover, the absence of porosity measurements or CT imaging prevented a direct correlation between changes in hydromechanical and mineralogical properties and microstructural alterations. Therefore, the objective of this work is to replicate the percolation experiments described by (Wang et al., 2010) and to identify the missing link between the hydromechanical behaviour and microstructural changes in Boom Clay under alkaline perturbation, with a particular focus on the self-sealing process.

The effects of ECW on the self-sealing capacity of the Boom Clay has already been studied in the frame of the TIMODAZ EC project in the temperature range of 20–80 °C (Chen et al., 2010). The results of the experiments showed that, after two months of interaction with ECW, the Boom Clay preserved its self-sealing capacity. The aim of the present study is to assess if this is still the case when Boom Clay is exposed to high pH solutions for extended time periods (several years).

In order to address this outstanding issue, Boom Clay samples were percolated with YCW and ECW for up to 5 years. After dismantling of the percolation cells, artificial planar fractures were created in the middle of the cores parallel and perpendicular to bedding planes. The assessment of self-sealing capacity was first done by measuring the evolution of the hydraulic conductivity of the fractured samples in presence of YCW and ECW in constant volume permeameter cells. Then, 3D imaging with the use of micro computed tomography (micro-CT) scanning and spectral X-ray computed micro tomography was used to evidence the closure of fracture by self-sealing. Finally, complementary post-mortem analysis involving QXRD (Quantitative X-ray diffraction analysis), SSA (specific surface area) and porosity measurements by N_2 – physisorption and FTIR (Fourier Transform Infrared) spectroscopy measurements were done to characterise self-sealing process. The novelty of this approach lies in the use of unique in-house developed experimental setups that enable hydromechanical and microstructural characterization of both intact and artificially fractured samples. To the best of our knowledge, spectral micro-computed tomography was employed for the first time in the investigation of argillaceous rocks considered as potential host formations for the geological disposal of radioactive waste.

2. Materials

The Boom Clay samples originate from the HADES drilled borehole CG72-73 W located in the Connecting Gallery between concrete rings 72 and 73 to the west at a distance of 19.50–20 m from the gallery lining (reference CG66-67 W core 20_section 20.2) and borehole TD 19–20 drilled vertically down in the Test Drift between concrete rings 19 and 20 (reference TD19–20, core 01–58, section 4.7–5.05 m). Both samples were located well beyond EDZ at the time of the sampling, thus they did not experience any mechanical damage prior to percolation tests and artificial fracturing. For the initial undisturbed Boom Clay, the rock samples from the same cores were crushed and used for the analysis. The initial water content in studied samples ranged between 18 and 20 wt%, as determined gravimetrically after drying at 110 °C. This water content corresponds to a fully saturated state in Boom Clay. The samples percolated by YCW parallel and perpendicular to bedding are hereafter denoted MiYo-1 and MiYo-2, respectively. In analogy, samples percolated by ECW parallel and perpendicular to bedding are hereafter denoted MiEvo-1 and MiEvo-2, respectively. The alkaline solutions were prepared in-house by dissolving 9.29 g of KOH, 1.89 g of NaOH and 0.16 g of $Ca(OH)_2$ in 1 L of outgassed Boom Clay pore water in the case of the YCW and 2,05 g of $Ca(OH)_2$ in 1 L of outgassed Boom Clay pore water in the case of the ECW following the procedure of (De Cannière et al., 1999). The final chemical composition of the feed waters used in the

percolation and permeameter cell tests along with the reference Boom Clay pore water composition as reported in (Honty et al., 2022) is provided in Table 1. For the (spectral) X-ray computed micro tomography imaging, the sample size was defined by internal dimensions of the permeameter cell, i.e. cylinder of 38 mm diameter and 32 mm height (Supplementary Fig. 1a). For the post-mortem analysis, i.e. SSA and porosity determinations, FTIR, and QXRD, subsample slabs approximately 1 cm thick were taken from the middle of the core, delineating the zone with the initial fracture (Supplementary Fig. 1b).

3. Experimental set-ups and methods

3.1. Percolation tests

The core samples were loaded into stainless steel percolation cells with internal diameter of 38 mm (Supplementary Fig. 2). The length of the sample was 32 mm in each cell. The sample was closed and confined within the cell by 2 stainless steel filters on inlet and outlet side, diameter 38 mm and 2 mm thickness, porosity 40 %. The porosity of the filters was chosen in such way as to comply with the diffusion accessible porosity (HTO) of the undisturbed Boom Clay (Aertsens et al., 2004). The sample within the percolation cell was subjected to a mean effective stress of 2.32 MPa, corresponding to a confinement pressure of approximately 23 bar, considering fully saturated sample. The inlet and outlet stainless steel pipes of 0.7 mm internal diameter served to feed YCW and ECW waters into the clay and collect percolate on the outlet side of the percolation cell. The constant percolation pressure of 8.12 ± 0.1 bar was maintained in each cell. The tests were performed in a temperature-controlled room at T of 20 °C (± 1 °C). The hydraulic conductivity was determined by Darcy's law as explained in section 3.3. The percolation experiments lasted for 2 years in case of the YCW and 5 years in case of the ECW. The difference in duration between YCW and ECW percolation and permeameter test runs was directly related to the faster attainment of steady hydraulic conductivity values in the former, whereas the latter required a longer period to reach steady-state conditions.

3.2. Creation of the fracture

The clay cores were recovered from the percolation cells by means of the hydraulic jack. The visual inspection of the sample showed no signs of desiccation, thus it was considered fully water saturated. Afterwards, the fracture was made in the core with the aid of stainless-steel hollow tube and knife sliding along grooves made on the sides of the tube. The core inserted in the tube was pushed against the blade of the knife with the aid of plunger and hydraulic press. The initial fracture network was quite irregular and extended the whole length of the core (Supplementary Fig. 3). The sample was then loaded into permeameter cell with the opening of the same diameter as that of the tube.

3.3. Permeameter cell set-up

The permeameter cells identical to those developed in the frame of the TIMODAZ EC project (Chen et al., 2010) were used for the purpose of the tests. The technical drawing of the permeameter cell is shown in Supplementary data file Fig. 4. Part of the top cap, part of the bottom base and the chamber of the permeameter cells were made of non-metallic Polycarbonate material. The reason for the use of polycarbonate is that it is more transparent to X-rays than metal, enabling fracture sealing under confined conditions to be visualized by micro-CT instruments. The clay plug with a diameter of 38 mm and height of 32 mm was enclosed in a cylindrical chamber under the same confinement pressure as in the case of the percolation experiment. The top and bottom metallic flanges were tightly screwed so that the volume of the sample remained constant. The top and bottom cap contained Teflon filters as to prevent potential clay erosion and clay loss into outflow solution. The outflow solution was collected in septum bottles with the aid of tubing and a needle perforating rubber cap. The second needle was pierced through the rubber cap in order to prevent pressure build-up in the bottle during water collection.

To determine hydraulic conductivity of fractured samples, the hydraulic pistons were filled with YCW and ECW of the same composition as during percolation tests. A syringe pump was used to control the pressure conditions and to measure the exact volume of injected YCW and ECW respectively. Although the pressure was imposed by the syringe pump, a pressure transducer (type DRUCK PTX 610) was placed between the hydraulic piston and the sample assembly and connected to the datalogger (Yokogawa MOBIDAQ) measuring continuously the real inlet pressure. The hydraulic conductivity calculation is based on Darcy's law:

$$K = \frac{Q \times \rho \times g \times L}{A \times P}$$

where Q is flow rate (m^3/s), ρ is liquid density (kg/m^3), g is gravitational acceleration (m/s^2), L is the length of the sample (m), A is the cross-sectional area (m^2), P is the pressure (bars) and K is the hydraulic conductivity (m/s). The permeameter cell tests were carried out at T of 20 °C (±1 °C) in the temperature-controlled room. In total, 219 hydraulic conductivity measurements were collected for module MiYo-1, 175 for MiYo-2, 418 for MiEvo-1, and 311 for MiEvo-2. The lower number of measurements in the cores percolated perpendicular to bedding reflects relatively lower flow rates in those cores. Each K-value typically represents an average flow rate over a period of 3–5 days. The typical measurement error for hydraulic conductivity determinations, whether from percolation or permeameter tests, is approximately 20 %.

Table 1
Composition of the reference Boom Clay pore water and alkaline solutions used in the percolation and permeameter cell tests. *from Honty et al. (2022).

	Young Cement Water		Evolved Cement Water		reference Boom Clay Water*	
	$mg.L^{-1}$	analytical error	$mg.L^{-1}$	analytical error	$mg.L^{-1}$	analytical error
Al	1,18	± 0.12	< 0,2	–	0.05	± 0.04
Ca	6.9	± 0.7	410	± 40	2.4	± 0.99
Fe	1.06	± 0.11	< 0,02	–	0.31	± 0.42
K	5600	± 600	32	± 20	8.2	± 1.67
Mg	2.66	± 0.27	< 0,01	–	1.7	± 0.58
Na	1510	± 150	440	± 40	308	± 58
Si	12.0	± 1.6	1.3	± 1,0	5.3	± 2.39
Sr	0.070	± 0.012	0.298	± 0,031	0.06	± 0.02
Cl	30.9	± 0.8	25.0	± 0,6	20.1	± 4.5
NO3	< 0,5	–	3.15	± 0,33	<0.5	–
SO4	< 0,5	–	3.73	± 0,24	1.45	± 1.76
EC (mS/cm)	46.0	–	8.6	–	1.54	± 1.35
pH	13.5	± 0.2	12.6	± 0.2	8.5	± 0.4

3.4. QXRD of the randomly oriented bulk powders

The sample preparation prior to QXRD analysis followed the procedure published by (Środoń et al., 2001). The sediments were dried in the oven at 60 °C and gently hand-crushed using the agate mortar. Then, 2.7 g of a clay sample dried at 60 °C was loaded into the McCrone Mill, together with 0.3 g of ZnO, which acted as an internal standard in the quantification process. 4 mL of methanol was added to the sample holder and the grinding time was limited to 5 min in order to avoid amorphization during the grinding process. Afterwards, the slurry was transferred into a bowl with methanol. The slurry was again dried in the oven at 60 °C, the mixture was gently crushed and finally sieved to pass through a 63 μm sieve. The prepared mixture of sample/ZnO internal standard was subsequently side-loaded. The measurements of the side-loaded samples were performed with a Bruker D8 X-ray diffractometer in a Bragg-Brentano setup with CuKα radiation, Ni filter and LynxEye detector. The operational parameters of the device were set at 45 kV and 30 mA from 5 to 60°2θ with a step size of 0.02°2θ at 2 s per step.

The mineral identification and quantification was carried out with the use of the Profex software (Doebelin and Kleeberg, 2015) and BGMN (Rietveld refinement software) mineral database. The relative agreement between modelled and experimental patterns is evaluated based on the statistical parameters Rwp, Rexp, and an acceptance limit for X^2 as shown by convergence progress dialog window. The standard error of the quantification method for the minerals present in our sample set is usually below 1 wt% (Środoń et al., 2001).

3.5. QXRD of the preferentially oriented specimens

Prior to qualitative and quantitative XRD analysis of the separated <2 μm fraction, the samples underwent modified Mehra-Jackson treatment (Jackson, 1975; Mehra and Jackson, 1958). For the preparation of the oriented specimens, 40 mg of Ca-exchanged clay of the <2 μm fraction was mixed per 1 mL of deionized water. The dispersion was pipetted on the glass slide and left to evaporate. 3.5 mL of the dispersion per glass slide of 8 cm^2 was generally enough to meet the infinite crystal thickness criterion (Moore and Reynolds, 1997). The slides were scanned in air-dry state (AD) and after saturating overnight at 60 °C with ethylene-glycol (EG). The diffractogram acquisition occurred with Bruker D8 advance using following instrumental settings: Bragg-Brentano geometry, Cu-source, primary and secondary Soller slits 2.5°, angular range: 2.9–47°2θ, step size: 0.04°2θ, time/step: 192 s, Lynxeye XE-T detector.

Patterns of preferred oriented specimens were processed with Sybilla (Chevron ETC proprietary software) to quantify the detailed clay mineralogy (Aplin et al., 2006; Mystkowski et al., 2002). Sybilla allows the calculation and combination of theoretical patterns of discrete and interstratified clay mineral models. The modelling strategy, the model mineral selection and fine-tuning of the input parameters specifically for Boom Clay were discussed in detail by (Zeelmaekers et al., 2015) and (Frederickx et al., 2021).

3.6. Specific surface area (SSA) and porosity

SSA measurements were performed with the use of a Micromeritics Tristar II 3020 surface area analyser and liquid N_2 ($T = 77$ K) as the adsorbate. SSA was determined using the BET (Brunauer-Emmett-Teller) equation (Brunauer et al., 1938). Prior to analysis, the powdered samples were degassed at a temperature of 110 °C for 24 h. The quantities of the monolayer adsorbed gas (Qm) were calculated from the slope and intercept of the linear part of the adsorption isotherms in the region of 0.05–0.2 P/P_0 relative pressure. The pore size distributions were determined from desorption data by BJH method (Barrett et al., 1951).

3.7. FTIR

FTIR in the middle infrared region (4000–400 cm^{-1}) were obtained on a Tensor-II Fourier transform infrared spectrometer from Bruker in transmission mode. The KBr pressed pellets were prepared by homogenizing 350 mg of KBr and 3 mg of grind sample and hydraulic press at 10 tons. The obtained spectra are averages of 500 scans with the resolution of 4 cm^{-1}. The spectra acquisition occurred at constant T and relative humidity conditions. Spectra manipulations were performed using the OPUS 8.5 software.

3.8. (Spectral) X-ray computed micro tomography

A combination of 3D micro-CT imaging and 2D spectral tomography was opted as optimal technique to i) visualize fractured zone, ii) follow the self-sealing process, iii) trace potential porosity clogging due to precipitation of secondary minerals and iv) gain insight into chemical information of the region of interest. The working principle of conventional μCT imaging can be found in (Cnudde and Boone, 2013) and that of spectral tomography in (Sittner et al., 2021). The conventional micro-CT scans of samples MiYo-1, MiYo-2, MiEvo-1 and MiEvo-2 were acquired at UGCT (University of Gent Centre for X-ray Tomography, Belgium). The combined μCT and spectral imaging was carried out only for MiEvo-1 and MiEvo-2 samples at DMEX (Development of the Experimental Methodologies for X Ray Imaging), Université de Pau et des Pays de l'Adour (France). In Gent, scans were acquired on the HECTOR system (Masschaele et al., 2013) using a directional high-power tube head in combination with a flat panel detector. In both measurement campaigns, the cylindrical-shaped samples were scanned inside permeameter cell, as shown in Supplementary Fig. 1a. The instrumental settings were the following: tube voltage 180 keV, tube current 250 W, 1 mm Al filter, voxel size 45 μm. The applied voltage was proportional to the sample's geometry, size, and target resolution. The image segmentation and beam hardening correction was performed using Octopus (version 8.8.0.15), a software suite developed by the Radiation Physics group at the Centre for X-ray Tomography (UGCT), Ghent University (Vlassenbroeck et al., 2007) The beam hardening correction was applied to compensate for the cylindric shape of the samples with no additional filtering of the data.

In Pau, the samples embedded in the polycarbonate cells were scanned using Tescan UniTom XL system, which combines micro-CT imaging (flat panel CT detector) with spectral X-ray imaging using a photon counting line detector with a CdTe sensor. The spectral CT is frequently used to differentiate materials with similar X-ray attenuation, based on the variations in their (average) atomic number and densities. The working principles and geological applications of this technique can be found in (Martini et al., 2021). The initial selection of region of interests was scanned with conventional micro-CT with the following settings: voxel size 52 μm, voltage 170 keV, target power 52 W, 0.75 mm Sn filter, 1146 projections over 360° range, time acquisition 79 min. The voxel size of 52 μm enabled the entire sample volume to be in the field of view. The same voxel size was used for conventional and spectral scans, respectively. The spectral tomography slice was acquired, operating the X-ray source at 160 kV and a target power of 15 W. A series of 1201 angular projections were collected over a 360° sample rotation. The total acquisition time was 30 min and the reconstructed voxel size 52 μm/voxel. The reconstructed linear attenuation coefficient at each voxel is comprised of 140 equidistant energy bins of 1 keV between 20 and 160 keV. Again, the voxel size of the spectral scan was selected in order to cover the full cross-section of the sample.

The data acquisition and image reconstruction were carried out by Acquila and Panthera software (both licensed softwares of Tescan) and Spectral Suite v 2.1.0.108 for spectral processing. The 3D reconstruction and image processing were done by Dragonfly software (Comet Technologies Canada Inc.)

4. Results and interpretation

4.1. Evolution of the hydraulic conductivity

In the undisturbed Boom Clay samples retrieved from borehole CG72-73 W, the hydraulic conductivities (*K*-value) were estimated at the start of the percolation experiment (*K*-value start percolation in Table 2) equal to 3.87× 10^{-12} m/s and 3.72 × 10^{-12} m/s in the module MiYo-1 and MiEvo-1, respectively (Fig. 1, Fig. 2 and Table 2). The *K*-values in the samples taken from the borehole TD19–20 were estimated at the beginning of the percolation tests to be about 1.35× 10^{-12} m/s and 5.32 × 10^{-13} m/s in the modules MiYo-2 and MiEvo-2, respectively. These initial *K*-values are generally in line with the reported K-value ranges determined for the Boom Clay in the laboratory and in-situ experiments at the Mol site (1.5–8 × 10^{-12} m/s) (Yu et al., 2013) with vertical *K*-values (K_V) lower than the horizontal ones *K* (K_H), and an anisotropic ratio *K*h/*K*v of about 2.5 (Yu et al., 2013).

In the module MiYo-1 percolated with YCW parallel to bedding, one can notice an initial decrease in the *K*-values down to 2.58 × 10^{-12} m/s, followed by slight increase and eventually steady *K*-values levelling-off at 3.69 × 10^{-12} m/s at the end of the percolation test (*K*-value end percolation in Table 2). Similar pattern in the evolution of the hydraulic conductivity could be observed in case of the MiYo-2 module (perpendicular) with slight decrease of *K*-value down to 1.07 × 10^{-12} m/s followed again by increase of *K* up to 1.98 × 10^{-12} m/s at the end of the percolation test (Fig. 1).

Unlike Boom Clay cores percolated with YCW, the evolution of *K*-values of samples interacted with ECW show more stable behaviour. In the module MiEvo-1 percolated parallel with the bedding, the initial *K*-value of 3.72 × 10^{-12} m/s (*K*-value start percolation in Table 2) tends slightly but gradually decrease with the advancement of the percolation, reaching a minimum value of 2.53 × 10^{-12} m/s at the end of the test. The evolution of the hydraulic conductivity in the module MiEvo-2 is akin to MiEvo-1, but with lower magnitude. Here, initial *K* (*K*-value start percolation in Table 2) of 5.32 × 10^{-13} m/s again moderately decreases with the progress of the percolation. The final *K*-value at the end of the percolation reached a minimum of 4.27 × 10^{-13} m/s (Fig. 2).

After fracturing, the K-values (*K*-values fractured in Table 2) abruptly increased in every studied case. In case of the module MiYo-1, the hydraulic conductivity about doubled from 3.69 × 10^{-12} m/s to 8.67 × 10^{-12} m/s. In the cell MiYo-2, the K-value increased by the order of magnitude from 1.98 × 10^{-12} m/s to as high as 1.04 × 10^{-11} m/s. In the module MiEvo-1, the hydraulic conductivity increased from 2.53 × 10^{-12} m/s prior to fracturing to as high as 1.76 × 10^{-11} m/s after fracturing. Finally, the hydraulic conductivity raised from 4.27 × 10^{-13} m/s to a maximum of 5.5 × 10^{-12} m/s in case of the MiEvo-2 module. Beyond this moment, the hydraulic conductivity measurements were continued with the aim to trace self-sealing process. Fig. 1 and Fig. 2 show that hydraulic conductivity follows decreasing trend in each studied case. In case of the modules MiEvo-1 and MiEvo-2 (Fig. 2) and to a lesser extent in the module MiYo-2, the drop in the hydraulic conductivity is clear and consistent. In sample MiYo-1, the evolution of the hydraulic conductivity after fracturing is more fuzzy with scatter of hydraulic conductivity data. The reason for this unstable behaviour is not yet fully understood but might be related to greater mechanical damage during fracturing and consequently longer time needed for clay reconsolidation. In any case, the hydraulic conductivity clearly decreased from 8.67 (*K*-value fractured in Table 2) to 5.45 × 10^{-12} m/s (*K*-value sealed in Table 2), 1.04× 10^{-11} m/s to 3.59 × 10^{-12} m/s in the modules MiYo-1 and MiYo-2. The relative decrease in *K*-values is even more pronounced in case of the samples percolated with ECW. The

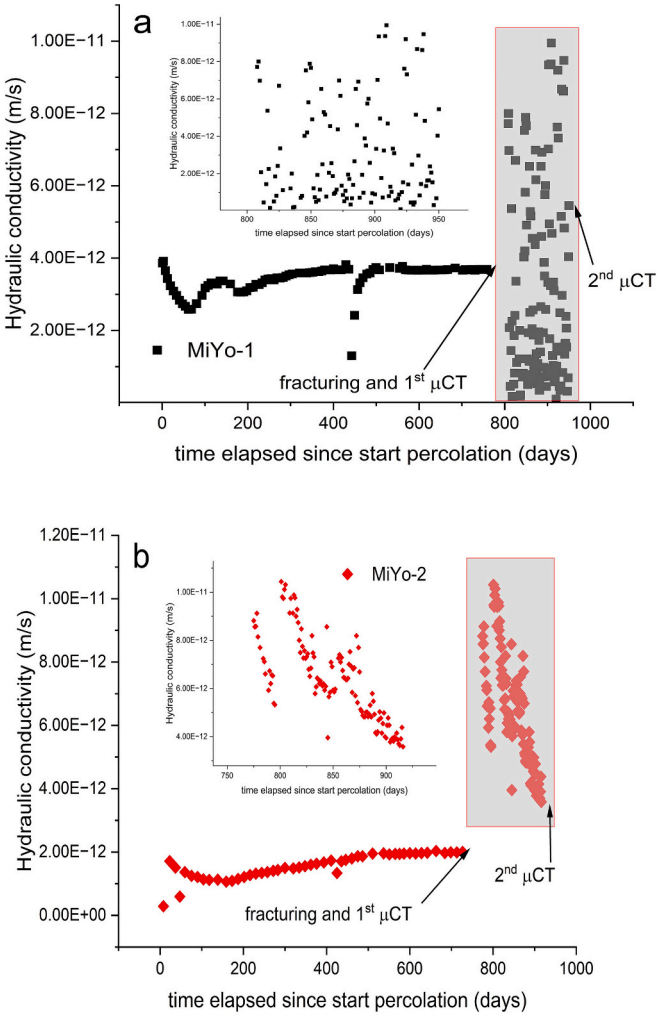

Fig. 1. Evolution of the hydraulic conductivity in the Young Cement Water (initial pH of 13.2) environment. Boom Clay samples percolated parallel (MiYo-1, a) and perpendicular (MiYo-2, b) to bedding. The moments of the µCT measurement campaigns are indicated by black arrows. Magnified views of the shaded regions are presented as graph insets.

Table 2
Overview of the hydraulic conductivity values of the undisturbed (K-value start percolation), fractured and sealed BC samples percolated by YCW and ECW.

Sample orientation	medium	*K-value* start percolation	*K-value* end percolation	*K-value* fractured*	*K-value* sealed
		(m/s)	(m/s)	(m/s)	(m/s)
II to bedding	YCW	3.87 × 10^{-12}	3.69 × 10^{-12}	8.67 × 10^{-12}	5.45 × 10^{-12}
⊥ to bedding	YCW	1.35 × 10^{-12}	1.98 × 10^{-12}	1.04 × 10^{-11}	3.59 × 10^{-12}
II to bedding	ECW	3.72 × 10^{-12}	2.53 × 10^{-12}	1.76 × 10^{-11}	6.61 × 10^{-12}
⊥ to bedding	ECW	5.32 × 10^{-13}	4.27 × 10^{-13}	5.5 × 10^{-12}	7.65 × 10^{-13}

* maximum measured K-value is reported here.

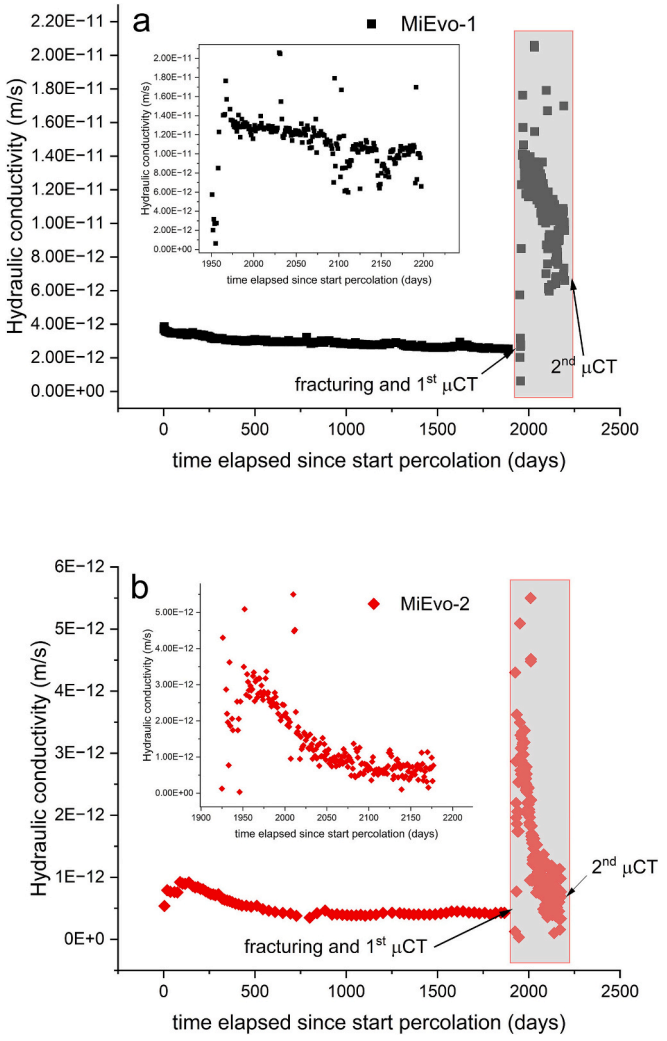

Fig. 2. Evolution of the hydraulic conductivity in the Evolved Cement Water (initial pH of 12.5) environment. Boom Clay samples percolated parallel (MiEvo-1, a) and perpendicular (MiEvo-2, b) to bedding. The moments of the µCT measurement campaigns are indicated by black arrows. Magnified views of the shaded regions are presented as graph insets.

hydraulic conductivity decreased from 1.76×10^{-11} m/s to 6.61×10^{-12} m/s and from 5.5×10^{-12} m/s to 7.65×10^{-13} m/s in case of the Boom Clay percolated parallel and perpendicular to bedding, respectively. Overall, the evolution of the hydraulic conductivity after fracturing strongly suggests that self-sealing process is still effective, even after several years of the interaction between Boom Clay and highly alkaline solutions.

It should be recalled at this point that several factors might have affected fluid transport through Boom Clay after interaction with the alkaline solutions prior to fracturing. Perhaps the most influential is the porosity change due to mineral dissolution and/or precipitation. The previous long-term percolation experiments employing Boom Clay and highly alkaline solutions (Wang et al., 2010) have shown hydraulic conductivity increase (about a factor of two) in the YCW environment and *K* decrease in the ECW environment (about 20 %). The increase in the hydraulic conductivity in the case of YCW was explained by dissolution of swelling clays and natural organic matter (based on XRD, UV-VIS and Dissolved Organic Carbon content analysis) thereby liberating a part of the pore space for fluid transport. In contrast, the decrease in the hydraulic conductivity in the case of ECW was tentatively attributed to porosity occlusion as a result of precipitation of the secondary calcite. Although no secondary calcite could be detected by mineralogical analysis, its precipitation was predicted by geochemical modelling. The chemistry of the percolate resulting from Boom Clay–alkaline plume interaction is beyond the scope of this study. For a detailed discussion on solute chemistry and related geochemical modelling, the reader is referred to the work of Wang et al. (2010).

4.2. *Specific surface area and porosity*

N_2-adsorption derived specific surface area as calculated from the linear part of the adsorption curves in the pristine samples TD19–20 and CG72-73 W were 30.5 ± 0.06 and 39.9 ± 0.17 m^2/g for the bulk clay. The specific surface area of the post-mortem samples MiYo-1 and MiYo-2 were 23.7 ± 0.02 and 21.6 ± 0.03 m^2/g, respectively. The samples MiEvo-1 and MiEvo-2 rendered identical SSA values of 24.4 ± 0.08 m^2/g. Though the heterogeneity of the initial samples with respect to SSA is significant, in all studied cases, the decrease of the specific surface area is evident. It follows that SSA decrease is more pronounced in samples treated with YCW than in samples treated with ECW. The sorption isotherms and pore size distributions of studied samples are shown in Fig. 3a and Fig. 3b, respectively. Fig. 3b indicates that specific surface area decrease is accompanied by relative shift of the mean pore size towards larger values. The maximum N_2-gas adsorption is reached for pore diameter of 4.04 nm in the undisturbed sample TD19–20, while it is 4.00 nm in case of the undisturbed sample CG72-73 W. The results indicate that positive shift of the pore size distribution towards larger pores is evident for all samples but no apparent relation could be established between the magnitude of the shift and either type of the

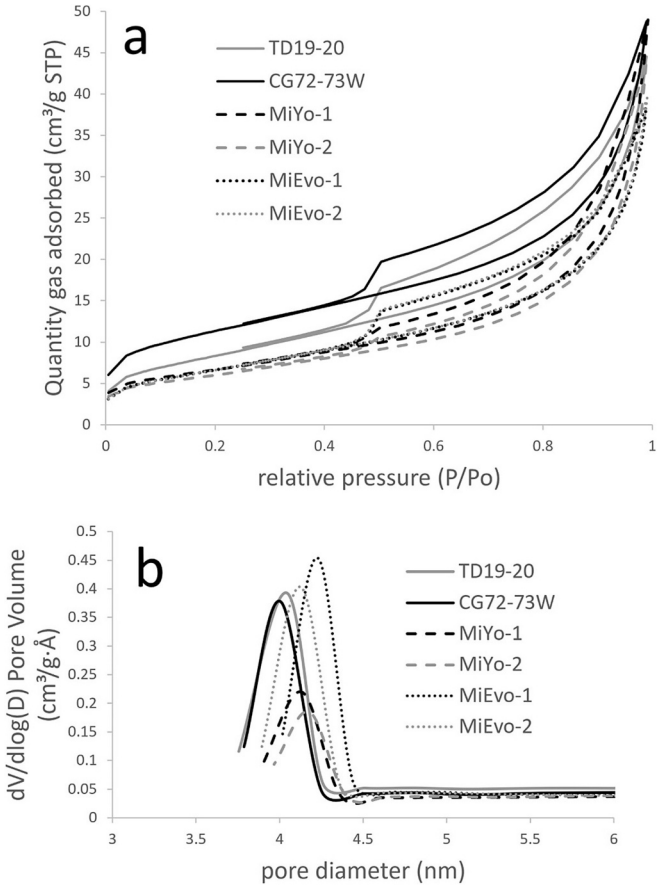

Fig. 3. (a) Sorption isotherms of the N_2 gas of the initial undisturbed Boom Clay samples (solid lines) and samples percolated with YCW (dashed lines) and ECW (dotted lines). MiYo-1 and MiEvo-1 – samples percolated in the direction parallel to bedding, MiYo-2 and MiEvo-2 – perpendicular to bedding. (b) pore size distribution of the analogous samples.

Table 3
Quantitative mineralogical composition of the bulk rocks as determined by Profex.

	TD19–20	CG72-73 W	MiYo-1	MiYo-2	MiEvo-1	MiEvo-2
Anatase	1.7	1.3	1.5	1.4	1.3	1.6
Calcite	1.0	2.5	6.1	1.6	4.1	1.0
Clinochlore	4.8	3.1	5.0	4.3	5.4	4.8
Kaolinite	8.4	8.2	7.7	8.2	7.6	9.2
K-feldspar	6.2	5.7	6.1	5.9	5.7	5.6
Muscovite/Illite /glauconite	20.7	19.6	21.7	20.5	19.6	20.2
Smectite	17.5	20.6	14.2	18.2	20.9	14.5
Plagioclase	8.9	9.2	10.8	11.1	10.3	13.7
Pyrite	3.6	2.5	1.5	3.4	3.7	2.1
Quartz	27.1	25.9	25.2	25.5	20.7	26.5
SUM 2:1 clays	38.2	40.2	35.9	38.7	40.5	34.8
Weighted total	100.0	98.6	100.0	100.0	99.5	99.3

All values in wt%. CG72-73 W and TD19–20 – undisturbed Boom Clay core samples. MiYo-1 and MiEvo-1 - post mortem samples originated from CG72-73 W core, MiYo-2 and MiEvo-2 – post mortem samples originated from TD19–20 core.

alkaline solution or bedding plane orientation. The maximum shift was documented in case of the MiYo-2 sample percolated perpendicular to the bedding planes from the mode porosity of 4.04 nm in undisturbed sample to 4.18 nm, while increase from 4.00 nm to 4.23 nm was found in sample percolated with ECW parallel to bedding planes (MiEvo-1).

It is important to note that, due to their 3D complexity and broad range of the porosity sizes, no single porosity characterization technique can fully resolve the pore space of the fine grained argillaceous sediments such as Boom Clay. Previous studies (Hemes et al., 2015; Hemes et al., 2013) have shown that a significant portion of the water accessible porosity in Boom Clay lies below the practical pore resolution limits of the BIB-SEM (broad ion beam scanning electron microscopy), FIB-SEM (focused ion beam scanning electron microscopy) and even below the resolution of MIP (Mercury Injection Porosimetry), which has a lower resolution limit of approximately 3.6 nm in equivalent pore throat diameter.

Although the N_2-physisorption technique can provide pore size distribution in the mesopore range (2–50 nm), it may yield unrealistic results due to nitrogen gas penetration into micropores, as noted by (Kaufhold et al., 2016) and references therein. Nevertheless, the total pore volume determined by N_2 physisorption is considered reliable as is the intensity of the peak around ~4 nm, which appears to correlate with microporosity. At the same time, argon gas is generally preferred over nitrogen for the pore size distribution analysis in the micropore domain as it lacks permanent polar momentum (Seemann et al., 2025). Yet, despite the known differences in micropore volumes between the two adsorbates, the total pore volumes and BJH-derived pore size distributions can be obtained from the physisorption isotherms of both gases (Seemann et al., 2025).

Despite the apparent limitations of the adopted methodology for pore size analysis, the current approach allows for inter-sample comparison, independent of absolute values (Kaufhold et al., 2016). Notably, the intensity of the peak maximum is lowest in the YCW environment (Fig. 3b), which indirectly indicates a partial loss of microporosity—likely due to smectite dissolution under high pH conditions. In this context, N_2-physisorption method was employed to trace potential porosity change inherent to clay matrix, while μCT was used to follow the self-sealing at the macro scale (>45 μm resolution).

The decrease in the specific surface area corroborates with the partial dissolution of the smectite in high pH environment, (e.g., Bauer and Velde, 1999; Honty et al., 2010; Nakayama et al., 2004; Ramirez et al., 2005). Nevertheless, it is important to mention that smectite dissolution was confirmed in the YCW environment, while its dissolution was not observed in the ECW solutions, irrespectively of the core orientation (Table 4 and section 4.3.2).

4.3. (Q)XRD analysis

4.3.1. QXRD of the bulk rocks

Normalized quantitative mineralogical composition of the whole rock samples as determined by fitting of the experimental patterns with the minerals from the BGMN database by Profex is shown in Table 3. Due to similarity of the diffractograms of both undisturbed and post-mortem samples (Fig. 4), all experimental patterns were fitted by the same set of 10 minerals (as refinement preset) next to ZnO used as internal standard. These minerals are anatase, calcite, clinochlore (Mg-chlorite), kaolinite, K-feldspar, plagioclase, mica, glauconite, pyrite and smectite. It should be noted that at the level of the whole rock analysis, the quantities of the individual 2:1 minerals (illite/muscovite, mixed layer I—S and smectite) is rather indicative.

In general, the quantitative mineralogical composition of the undisturbed Boom Clay samples (TD19—20 and CG72-73 W) fall within the range of values reported by (Zeelmaekers et al., 2015). Based on the study of (Zeelmaekers et al., 2015) the Boom Clay at the Mol site is composed of 21–59 wt% quartz, 4–10 wt% K-feldspar, 0.7–4 plagioclase, 0–4 wt% calcite, 0.5–3 wt% pyrite, 0.4–1 wt% anatase, 3–16 wt%

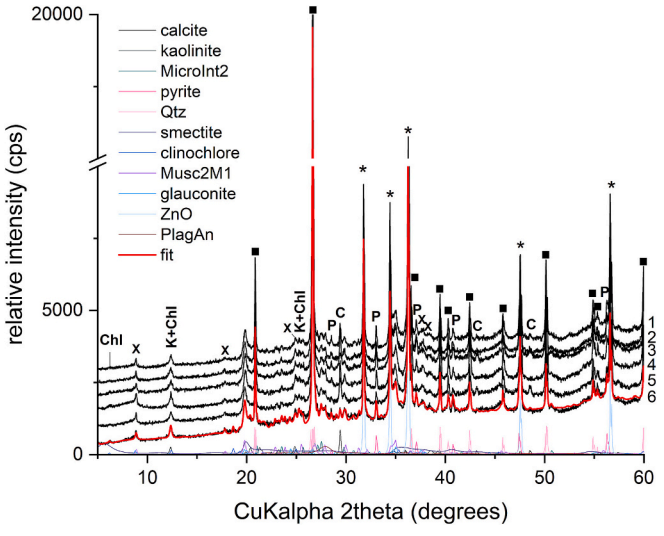

Fig. 4. XRD patterns of the whole-rock randomly oriented powders. From top to the bottom, sample CG72-73 W (1), TD19–20 (2), MiEvo-1 (3), MiEvo-2 (4), MiYo-1 (5) and MiYo-2 (6). Example of the modelled pattern in Profex (red), Chl- chlorite, x – illite/Muscovite 2 M1, K – kaolinite, P – pyrite, C – calcite, quartz – black boxes, ZnO – asterisks. (For interpretation of the references to colour in this figure legend, the reader is referred to the web version of this article.)

Table 4
Quantitative mineralogical composition of the <2 μm fraction of the studied samples.

	CG 72-73 W		TD19–20		MiYo-1		MiYo-2		MiEvo-1		MiEvo-2	
	AD	EG	AD	EG	AD	EG	AD	EG	AD	EG	AD	EG
Smectite	22.2	22.3	23.7	17.6	21.5	16.6	16.1	13.6	26.7	20	22.8	20.1
IS	37	35.5	33.3	37.9	44	44.1	30.2	34.1	39.4	44.1	36.3	36.6
%I in I-S	69	66	71	71	72	69	72	69	78	69	68	68
Illite	16.8	17.2	17.9	18.2	15	16.4	26.3	24.6	11.3	12.8	15.5	17.3
Kaolinite	5.4	4.2	6.8	8.8	4.9	2.8	10.4	7.9	3.5	5.2	6.5	4.9
KS	15.1	17	14.9	12.6	12	18.2	12.9	16.1	12.9	14.4	16.4	18.9
%K in K-S	79	84	80	84	82	86	79	82	79	82	79	86
Chlorite	3.5	3.9	3.3	5	2.7	1.8	4.2	3.7	6.2	3.5	2.5	2.1
Smectitic	37	37	36	31	36	33	27	27	38	36	38	34
Illitic	42	41	42	45	47	47	48	48	42	43	40	42

AD – air dry, EG – ethylene-glycol state, IS – mixed layer illite-smectite, I-illite, KS – mixed layer kaolinite-smectite, K – kaolinite. All values in wt%. CG72-73 W and TD19–20 – undisturbed Boom Clay core samples. MiYo-1 and MiEvo-1 - post mortem samples originated from CG72-73 W core, MiYo-2 and MiEvo-2 – post mortem samples originated from TD19–20 core.

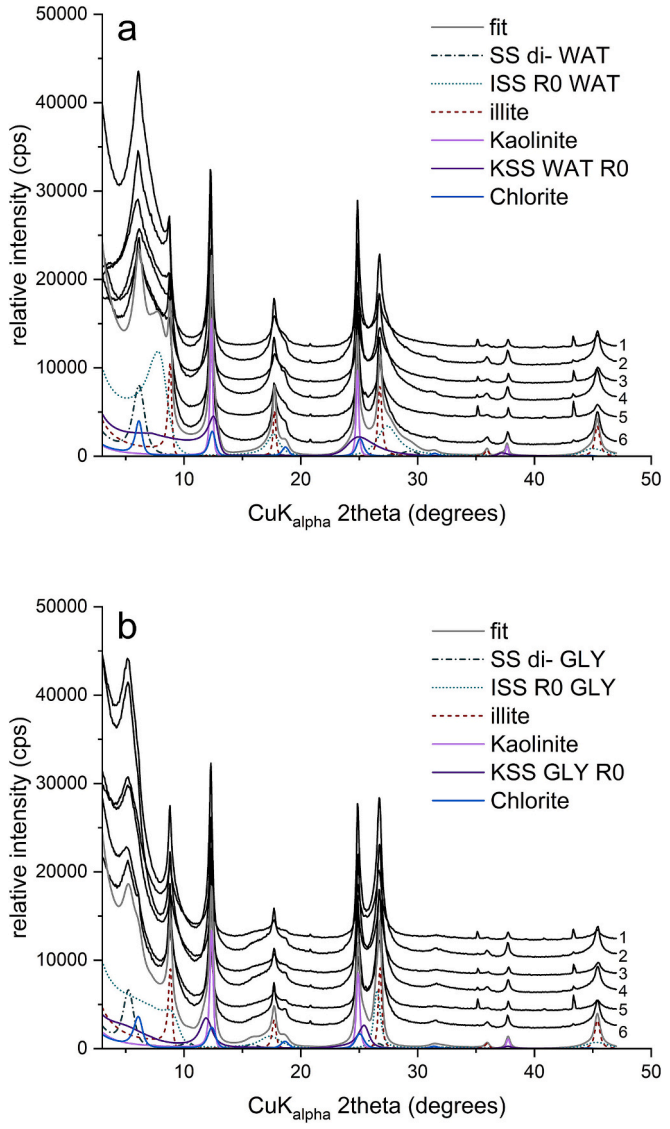

Fig. 5. X-ray diffractograms of the oriented patterns in air-dry (a) and ethylene-glycol state (b). From top to the bottom sample CG72-73 W (1), TD19–20 (2), MiEvo-1 (3), MiEvo-2 (4), MiYo-1 (5) and MiYo-2 (6). Example of the modelled pattern in Sybilla (grey). SS – smectite with high charge and low charge component, ISS R0 – randomly ordered mixed layer illite-smectite, KSS R0 – randomly ordered mixed layer kaolinite-smectite.

kaolinite and 1–4 wt% chlorite. The sum of 2:1 clay minerals attains 22–56 wt%. Next to calcite, also siderite and dolomite can be present in minute amounts (up to 0.5 wt%), but not systematically in every and each sample. In this study, the quantities of anatase and plagioclase systematically exceed the reported value ranges. The reason might be related to structural difference in the selected minerals and/or quantification approach (Quanta in the first case and Profex in this study). However, such discrepancy is of minor importance in the studied context. The variation in the mineralogical composition between undisturbed samples is limited and reflects natural heterogeneity of the Boom Clay for the sampled depth interval.

4.3.2. QXRD of the preferentially oriented clay fraction specimens

The results of the quantitative analysis of the <2 μm fraction as performed by Sybilla modelling can be found in Table 4 and Figs. 5a (air-dry) and Fig. 5b (ethylene-glycol state). The modelling was deemed successful when the quantitative results of the fitting in the air-dry and glycolated state gave comparable results. For the modelling of the undisturbed Boom Clay samples, we used the same mineral combination as suggested by (Zeelmaekers et al., 2015), i.e. 6-component model composed of discrete smectite (SS), mixed layer illite-smectite (ISS R0), illite, kaolinite, mixed layer kaolinite-smectite (KSS) and chlorite. The notion of two "SSs" in the code refers to two types of smectitic layers in the interstratified IS, namely high charge and low charge component to account for the heterogeneities in the swelling behaviour (for detailed discussion see (Zeelmaekers et al., 2015). The proportion of the low charge smectite in the interstratified phases and discrete smectite with respect to high charge component varies between 0.65 and 0.75 based on the modelling. The mixed layer I—S is highly illitic with about 66 to 71 % of illitic layers in the EG state. The mixed layer KSS is highly kaolinitic with 82 to 86 % of kaolinite in the mixed layer structure (Table 4). Overall, the proportions of the components within the mixed layers remain remarkably stable among the studied samples.

The comparison of the diffractograms and quantitative mineralogical results of the undisturbed and reacted samples shows that no significant mineralogical changes occurred as a result of Boom Clay-alkaline plume interaction over the period of ~5 years. The only significant change is observed in sample MiYo-2 percolated with Young Cement Water in the direction perpendicular to the bedding planes. Here, the partial dissolution of smectite did occur based on the analysis of <2 μm fraction. The maximum decrease in the smectite content is about 10 wt%. Strikingly, the largest change in the porosity was documented in the same MiYo-2 sample. The results of the mineralogical analysis agree well with the previous findings of (Honty et al., 2010) where partial dissolution of smectite was observed in Boom Clay in YCW environment but no dissolution was detected in samples interacted with ECW.

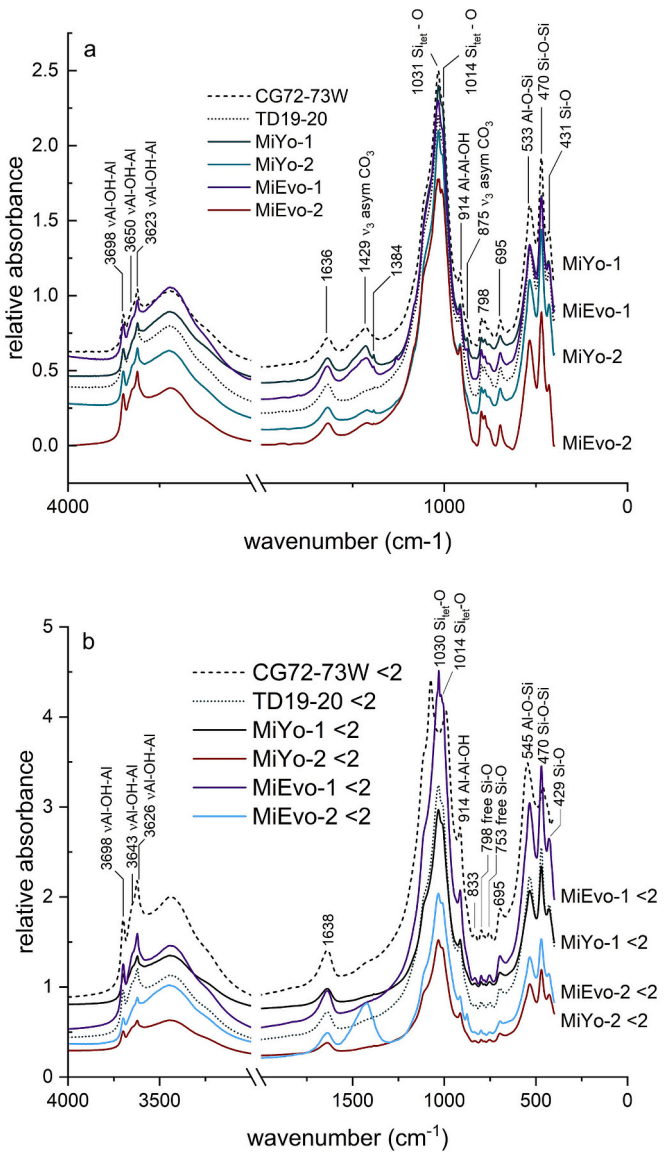

Fig. 6. FTIR spectra of bulk (a) and < 2 μm fraction post-mortem samples (b) in the mid-infrared region.

4.4. FTIR

Because of the many similarities in the mid-infrared region spectra of the bulk rocks and separated clay fractions of the studied samples, they are discussed together here. The spectra measured in the transmission mode are shown in Fig. 6a for the bulk rocks and Fig. 6b for the clay fraction. In the OH stretching region (4000 to about 3500 cm^{-1}), well resolved band at 3623 (bulk) and 3626 cm^{-1} (<2 μm) respectively, can be assigned to inner hydroxyl groups of kaolinite, positioned between the tetrahedral and octahedral sheets. A strong band at 3698 cm^{-1} is related to the in-phase symmetric stretching vibration of the OH groups of the octahedral sheets, whereas out-of-plane OH stretching vibrations are typical for a band at ~3650 cm^{-1} (Madejová, 2003). A broad band near 3430 cm^{-1} observed clearly in all studied spectra is related to H-O-H vibrations of adsorbed water in smectite. It is worth mentioning that the exact position of this band depends both on the relative humidity and interlayer cation (Kuligiewicz et al., 2015).

The Si—O stretching vibrations at 1030 and 1014 cm^{-1} can be assigned to contributions of the Si—O bonds in the tetrahedral sheets of kaolinite, dioctahedral smectite (montmorillonite in this case) or illite. The sharp well resolved peak at 914 cm^{-1} is diagnostic for Al_2OH bending bands of kaolinite and arise from vibrations of inner and surface OH groups, respectively (Madejová, 2003). In the low end of the middle infrared region, the band at 533 cm^{-1} (bulk) and 544 cm^{-1} (<2 μm) originate from variable contributions of Si-O-Al (octahedral Al) in the clay minerals, whereas the band at 470 cm^{-1} present in the spectra of both bulk rocks and < 2 μm fractions arise from Si-O-Si bending vibrations.

The most significant difference between FTIR spectra of the bulk rocks and separated clay fraction is the presence of the bands at 1429 and 875 cm^{-1} in the first and their absence in the latter case (Fig. 6a and b). These bands can be attributed to asymmetrical vibrations of CO_3 groups in calcite (Rodriguez-Blanco et al., 2010; Russell and Fraser, 1994; Tatzber et al., 2007). They were observed in the undisturbed sample CG72-73 W and corresponding samples MiYo-1 and MiEvo-1 percolated with YCW and ECW in the direction parallel to bedding (Fig. 6a). Relative increase of the calcite content in samples MiYo-1 and MiEvo-1 compared to initial material is also suggested by QXRD analysis. (Table 3). Nevertheless, calcite was not detected by micro-CT imaging, likely due to the limited resolution (45 μm). Although both QXRD and FTIR indicate possible calcite precipitation in the MiYo-1 and MiEvo-1 samples, further investigation is required to confirm carbonation. Calcite precipitation in Boom Clay under ECW conditions was predicted by geochemical modelling (Wang et al., 2010), however, no mineralogical evidence was found in the post-mortem samples to support this process.

In summary, FTIR spectra of the undisturbed and post mortem samples indicate that, aside from potential calcite precipitation, no significant dissolution, precipitation or mineralogical transformation occurred as a result of clay-alkaline solution interactions over the studied time period. These findings indicate a limited reactivity of the Boom Clay under the tested alkaline conditions.

4.5. X-ray computed micro-tomography (μCT) and spectral X-ray computed micro-tomography (SP-μCT)

In order to visualize the evolution of the sealing process in fractured samples, micro-CT was performed at distinct moments, i.e. state of the sample one day after fracturing and shortly after termination of the permeameter test (post-mortem). These distinct moments are indicated in Fig. 1 and Fig. 2. The first CT campaign took place after 758 and 727 days of the percolation with YCW in samples MiYo-1 and MiYo-2, respectively, corresponding to a percolation of 68 and 30 times the volumes of pores and fractures. In samples MiEvo-1 and MiEvo-2, the first CT scans were taken after 1888 and 1867 days of the percolation with the ECW corresponding to a percolation of 140 and 24 times of the pore volumes, respectively, followed by fracturing. The lower number of percolated volumes is inherent to relatively lower *K*-values observed in these specific samples. The second measurement campaign occurred after 950 days and 916 days in case of the MiYo-1 and MiYo-2 modules, whereas the permeameter cell tests lasted up to 2198 and 2177 days in the case of the MiEvo-1 and MiEvo-2 modules. Again, the rather long duration of the permeameter cell tests with ECW compared to YCW is related to the relatively lower *K*-values observed in the former than in the latter case.

The comparison of the selected regions of interest taken approximately at the mid-height of the studied cores from the first and second measurement campaigns is shown in Fig. 7 for samples MiYo-1 and MiEvo-1. Similar results were obtained for samples fractured in direction perpendicular to bedding (MiYo-2 and MiEvo-2, not shown). In addition to μCT images, also relative X-ray attenuation was measured across the profiles cross-cutting the fractured zone. As the linear attenuation coefficient μ along the X-ray path depends, next to atomic number Z and X-ray energy E, on the material density ρ, it can be used as good indicator of the sealing process. Indeed, there is clear difference in the relative X-ray attenuation determined perpendicular to fracture direction in samples right after fracturing and at the end of the test (Fig. 7

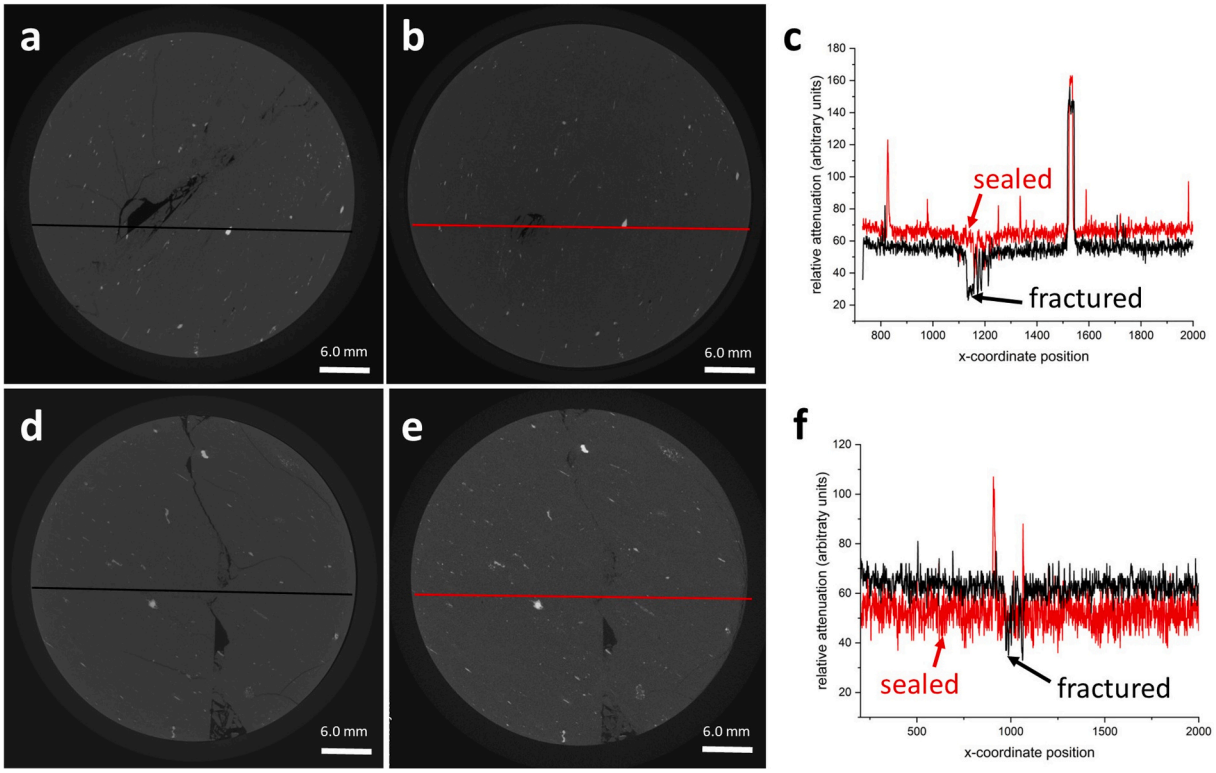

Fig. 7. μCt images of the MiYo-1 sample immediately after fracturing (a), after self-sealing (b), and corresponding X-ray attenuation profiles oriented perpendicular to the initial fracture (c). Similarly, for the MiEvo-1 sample: images taken immediately after fracturing (d), after self-sealing (e), and the corresponding X-ray attenuation profiles (f).

right). The X-ray attenuation profiles of fractured samples contain typical dip in the central part of the fracture thus reflecting lower density than the surrounding clay matrix. On the other hand, the X-ray attenuation of the post mortem samples show flat profiles, which points to limited density difference of the material. It is worth mentioning that locally, also increased X-ray attenuation is observed. These areas can be attributed to mineral grains of high density, like pyrite. Overall, the comparison of the μCT images and X-ray attenuation profiles of the fractured samples and samples at the end of the permeameter tests allows to conclude that Boom Clay retained its self-sealing capacity, even after extended periods of the percolation with both YCW and ECW.

To further investigate the cause of the fracture sealing, the modules MiEvo-1 and MiEvo-2 were studied by means of spectral micro-CT technique. The calcite precipitation in the ECW environment was experimentally observed and predicted by geochemical modelling in some earlier studies (e.g. Adler et al., 2001; Gaucher, 2005; Wang et al., 2010). Provided that density and Z effective of the secondary minerals and clay matrix can be successfully differentiated, SP-μCT can be useful to trace carbonation within the fracture zone. The Z effective represents the material composed of multiple elements as an artificial element which have similar attenuation coefficient.

As an example, Fig. 8 shows a 2D histogram of density versus Z effective corresponding to SP-μCT image and the SP-μCT image with superimposed segmented maps of phases present in the sample MiEvo-1. The points of the 2D histogram of density versus Z effective (Fig. 8a) correspond to all the pixels of SP-μCT image and show different clouds corresponding to clay matrix, fracture filling material and heavy minerals (anatase and pyrite) contained in the clay matrix. The selection of each cloud allows extracting each phase in the SP-μCT image which are presented on Figs. 8 b, c and d. The density and Z effective averages are respectively 1.99 ± 0.28 g/cm^3 and 12.6 ± 1.6 in the clay matrix, 1.41 ± 0.44 g/cm^3 and 10.41 ± 2.4 in the fracture material and 1.87 ± 0.39 g/cm^3 and 20.3 ± 7.61 in the heavy minerals. The bulk density of the clay matrix is consistent with the bulk density of the undisturbed Boom Clay (1.9 to 2.1 g/cm^3) reported elsewhere, e.g. (Bengtsson and Pedersen, 2016). If calcite precipitation occurred within the fracture zone, the Z effective should be closer to ~15 as theoretically calculated and measured by (Martini et al., 2021) for pure calcite mineral. Although the average density of the heavy minerals deviates significantly from the expected value for pyrite, the average Z effective is similar to that of pure pyrite (21.6) (Martini et al., 2021). The zones containing heavy minerals, however involve multiple elements in variable quantities, which explains the large error estimation concerning the Z effective.

Thus, the clay matrix and fracture filling material have common chemical composition with relatively lower density in the latter. The spectral CT data suggest that fracture sealing occurred as a result of creep behaviour of the clay (filling of the fracture voids with swelling clay minerals and secondary consolidation) rather than precipitation of the secondary minerals under the studied spectral resolution. Altogether, the spectral CT investigation corroborates the results of the mineralogical analysis and porosity measurements, which suggest no significant formation of the secondary minerals on one hand and tiny but detectable increase in the meso-porosity on the other hand. The porosity changes can be linked to partial dissolution of smectite in the YCW environment on one hand and plastic behaviour of the clay minerals effectively able to fill the void space of the fracture during the self-sealing process on the other hand.

5. Conclusions

Boom Clay samples were percolated with Young Cement Water (YCW) and Evolved Cement Water (ECW) solutions for up to five years. After this period, the samples were fractured and re-exposed to the same solutions to assess their self-sealing capacity (or lack thereof) following prolonged interaction with highly alkaline conditions. Self-sealing behaviour was monitored through hydraulic conductivity

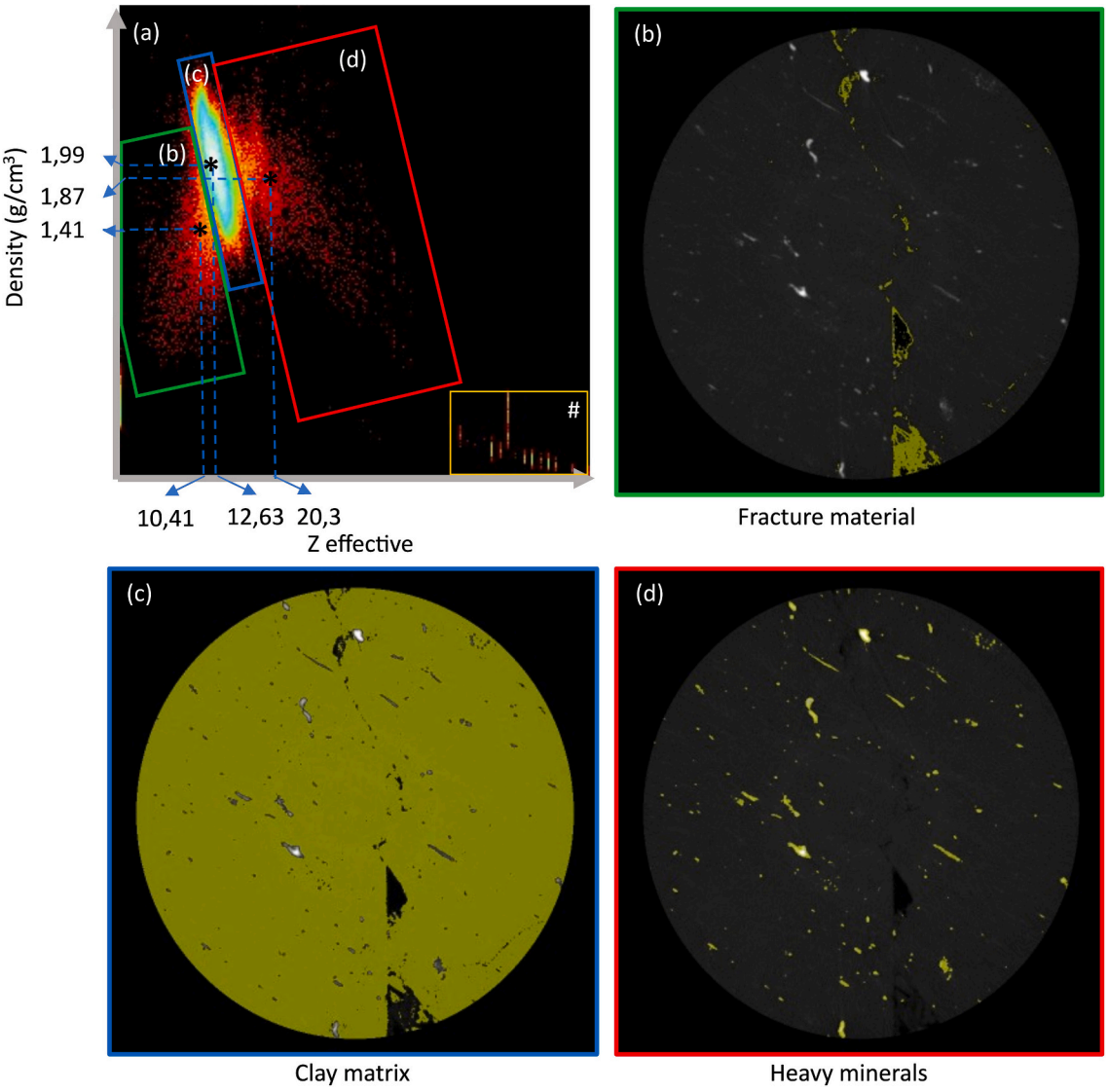

Fig. 8. 2D histogram of density versus Z effective of the SP-μCT image (a) and the SP-μCT image with superimposed segmented maps of fracture material (b), clay matrix (c) and heavy minerals (d). The segmented maps are obtained by selecting points of clouds present in (b), (c) and (d) rectangles corresponding respectively to fracture material, clay matrix and heavy minerals. The asterisk symbols on (a) represent the average of density and Z effective for each rectangle. The points of bottom right small rectangle (#) in (a) rectangle correspond to pixel of the image border and are not used for the analysis.

measurements in constant-volume permeameter cells, complemented by (spectral) micro-CT (Computer Tomography) imaging. In addition, specific surface area and pore size distributions were derived from N_2 gas physisorption in both the initial and post-mortem samples complemented by FTIR (Fourier Transform Infrared spectroscopy), and QXRD (Quantitative X-ray diffraction) analysis.

The initial hydraulic conductivity (K) values of the Boom Clay samples aligned with previously reported data from laboratory and in-situ experiments. Fracturing resulted in a significant increase in hydraulic conductivity across all samples, highlighting the structural impact. However, a self-sealing process was observed post-fracturing, with K-values gradually decreasing over time, irrespective of solution type or core orientation. This indicates that Boom Clay retains its self-sealing capacity even after extended exposure to highly alkaline solutions. Micro-CT images and relative attenuation profiles across fractures further support this self-sealing process.

N_2-physisorption tests of post-mortem samples revealed a decrease in specific surface area, accompanied by a decrease in microporosity in all cases. While the decrease in SSA can be attributed to partial smectite dissolution in the YCW environment, the increase of the mean pore size is likely linked to relative density changes near fractures and associated creep effects. The increase in the mean pore size corroborates with the overall rise in hydraulic conductivity compared to the initial state.

XRD and FTIR analyses showed no significant mineralogical transformations in most samples, except for a slight reduction in smectite content in samples percolated with YCW. Despite predictions from geochemical modelling in the earlier studies, secondary calcite precipitation could not be confirmed. This conclusion is further supported by dual-energy spectral maps and micro-CT data from ECW samples, which show that both the intact clay matrix and fracture fillings share the same chemical composition, though they exhibit varying bulk densities at the studied resolution. This study confirms self-sealing of Boom Clay under highly alkaline conditions extends and complements earlier observations on the self-sealing behaviour of similar host rocks for radioactive waste confinement (Barakat et al., 2024; Chen et al., 2014; Di Donna et al., 2022; Van Geet et al., 2008; Wang et al., 2024).

Credit authorship contribution statement

Miroslav Honty: Writing – review & editing, Writing – original draft, Investigation, Formal analysis, Data curation, Conceptualization. **Lander Frederickx:** Software, Methodology, Investigation, Formal analysis. **Ivan Josipović:** Visualization, Software, Methodology, Investigation, Formal analysis. **Matthieu N. Boone:** Writing – review & editing, Supervision, Methodology. **Pascale Senechal:** Writing – original draft, Visualization, Software, Methodology, Investigation, Formal analysis. **Stéphane Faucher:** Writing – review & editing, Software, Methodology. **Séverine Levasseur:** Writing – review & editing, Project administration, Funding acquisition. **Xavier Sillen:** Writing – review & editing, Project administration, Funding acquisition.

Declaration of Competing Interest

The authors declare the following financial interests/personal relationships which may be considered as potential competing interests:

Miroslav Honty reports financial support was provided by National Agency for Radioactive Waste and Enriched Fissile Materials. Miroslav Honty reports financial support was provided by European Commission. If there are other authors, they declare that they have no known competing financial interests or personal relationships that could have appeared to influence the work reported in this paper.

Acknowledgements

This project has received funding from the European Union's Horizon Europe research and innovation program under grant agreement No 101131765 (EXCITE2) for Transnational Access conducted at UPPA-DMEX, France. The work presented herein has been performed in the broader framework of a public-public cooperation between ONDRAF/NIRAS and SCK CEN. QMineral Analysis and Consulting bvba is acknowledged for the X-ray measurements of the oriented clay sample specimens.

Appendix A. Supplementary data

Supplementary data to this article can be found online at https://doi.org/10.1016/j.clay.2025.107911.

Data availability

Data will be made available on request.

References

Adler, M., Mäder, U.K., Waber, H.N., 2001. Core Infiltration Experiment Investigating High-pH Alteration of Low-Permeability Argillaceous Rock at 30°C, 10th International Symposium on Water-Rock Interaction. Villasimius, Italy, pp. 1299–1302.

Aertsens, M., Wemaere, I., Wouters, L., 2004. Spatial variability of transport parameters in the Boom Clay. Appl. Clay Sci. 26, 37–45.

Aplin, A.C., Matenaar, I.F., McCarty, D.K., van der Pluijm, B.A., 2006. Influence of mechanical compaction and clay mineral diagenesis on the microfabric and pore-scale properties of deep-water Gulf of Mexico mudstones. Clay Clay Miner. 54, 500–514.

Atkinson, A., Everitt, N.M., Guppy, R., 1989. Evolution of pH in a radwaste repository: Experimental simulation of cement leaching: Part 1. DOE/RW/89/025.

Barakat, Y., Mokni, N., Cui, Y.J., Delage, P., Bernier, F., 2024. Investigation of the self-sealing of Opalinus Clay from the lower sandy facies of Mont Terri site by mock-up tests with highly saline and alkaline solutions. Can. Geotech. J. 61, 189–207.

Barrett, E.P., Joyner, L.G., Halenda, P.P., 1951. The determination of pore volume and area distributions in porous substances. I. Computations from nitrogen isotherms. J. Am. Chem. Soc. 73, 373–380.

Bastiaens, W., Bernier, F., Li, X.L., 2007. SELFRAC: experiments and conclusions on fracturing, self-healing and self-sealing processes in clays. Phys. Chem. Earth 32, 600–615.

Bauer, A., Velde, B., 1999. Smectite transformation in high molar KOH solutions. Clay Miner. 34, 259–273.

Bengtsson, A., Pedersen, K., 2016. Microbial sulphate-reducing activity over load pressure and density in water saturated Boom Clay. Appl. Clay Sci. 132, 542–551.

Bernard, E., Jenni, A., Toropovs, N., Mäder, U., 2023. Percolation experiment across a 10-year-old interface between Opalinus Clay and Portland concrete. Cem. Concr. Res. 170.

Berner, U.R., 1992. Evolution of pore water chemistry during degradation of cement in a radioactive waste repository environment. Waste Manag. Nuclear Fuel Cycle 12, 201–219.

Bernier, F., Li, X.L., Bastiaens, W., 2007. Twenty-five years' geotechnical observation and testing in the Tertiary Boom Clay formation. Geotechnique 57, 229–237.

Bock, H., 2014. The OECD/NEA Report on Self-Sealing of Fractures in Argillaceous Formations in the Context of Geological Disposal of Radioactive Waste, 12th International IAEG Congress, Torino, ITALY, pp. 503–506.

Bossart, P., Trick, T., Meier, P.M., Mayor, J.C., 2004. Structural and hydrogeological characterisation of the excavation-disturbed zone in the Opalinus Clay (Mont Terri Project, Switzerland). Appl. Clay Sci. 26, 429–448.

Brunauer, S., Emmett, P.H., Teller, E., 1938. Adsorption of gases in multimolecular layers. J. Am. Chem. Soc. 60, 309–319.

Chen, G.J., Maes, T., Vandervoort, F., Silen, X., Van Marcke, P., Honty, M., 2010. Thermal impact on damaged argillaceous rocks: Permeameter test and Isostatic test on Boom Clay and Opalinus Clay from the TIMODAZ project. In: SCK-CEN-ER-145 Report, Mol, p. 42.

Chen, G.J., Maes, T., Vandervoort, F., Sillen, X., Van Marcke, P., Honty, M., Dierick, M., Vanderniepen, P., 2014. Thermal Impact on Damaged Boom Clay and Opalinus Clay: Permeameter and Isostatic Tests with μCT Scanning. Rock Mech. Rock. Eng. 47, 87–99.

Cnudde, V., Boone, M.N., 2013. High-resolution X-ray computed tomography in geosciences: a review of the current technology and applications. Earth Sci. Rev. 123, 1–17.

De Cannière, P., Dierckx, A., Moors, H., Wang, L., Aertsens, M., Lolivier, P., Put, M., Ortiz, L., Van Ravestyn, L., Van Gompel, M., Janssens, K., Maes, T., 1999. Migration studies, Tasks 2.1, 2.3 and 2.4, In: Geological disposal of conditioned high-level and long lived radioactive waste, progress report to NIRAS/ONDRAF for the second semester of 1997, SCK•CEN Report, R-3379, Mol, Belgium.

Di Donna, A., Charrier, P., Dijkstra, J., Ando, E., Besuell, P., 2022. The contribution of swelling to self-sealing of claystone studied through x-ray tomography. Phys. Chem. Earth 127.

Doebelin, N., Kleeberg, R., 2015. Profex: a graphical user interface for the Rietveld refinement program BGMN. J. Appl. Crystallogr. 48, 1573–1580.

Dolder, F., Mäder, U., Jenni, A., Schwendener, N., 2014. Experimental characterization of cement–bentonite interaction using core infiltration techniques and 4D computed tomography. Phys. Chem. Earth, Parts A/B/C 70-71, 104–113.

Fernández, R., Mäder, U., Rodríguez, M., de la Villa, R., Cuevas, J., 2009. Alteration of compacted bentonite by diffusion of highly alkaline solutions. Eur. J. Mineral. 21, 725–735.

Fernández, R., Cuevas, J., Mäder, U., 2010. Modeling experimental results of diffusion of alkaline solutions through a compacted bentonite barrier. Cem. Concr. Res. 40, 1255–1264.

Frederickx, L., Honty, M., De Craen, M., Elsen, J., 2021. Evaluating the quantification of the clay mineralogy of the Rupelian Boom Clay in Belgium by a detailed study of size fractions. Appl. Clay Sci. 201.

Gaboreau, S., Prêt, D., Tinseau, E., Claret, F., Pellegrini, D., Stammose, D., 2011. 15 years of in situ cement-argillite interaction from Tournemire URL: Characterisation of the multi-scale spatial heterogeneities of pore space evolution. Appl. Geochem. 26, 2159–2171.

Gaucher, E., 2005. Modeling diffusion of an alkaline plume in two types of clayey systems. In: ECOCLAY II: Effects of Cement on Clay Barrier Performance - Phase II. Final Report, EC project n°FIKW-CT-2000-00028 ; Andra report n°CRPASCM04–0009, p. 381.

Gonzalez-Blanco, L., Romero, E., Levasseur, S., 2024. Self-Sealing of Boom Clay after Gas Transport. Rock Mech. Rock. Eng. 57, 4173–4189.

Hemes, S., Desbois, G., Urai, J.L., De Craen, M., Honty, M., 2013. Variations in the morphology of porosity in the Boom Clay Formation: insights from 2D high resolution BIB-SEM imaging and Mercury injection Porosimetry. Netherlands J. Geosci. Geologie En Mijnbouw 92, 275–300.

Hemes, S., Desbois, G., Urai, J., Schröppel, B., Schwarz, J., 2015. Multi-scale characterization of porosity in Boom Clay (HADES-level, Mol, Belgium) using a combination of X-ray μ-CT, 2D BIB-SEM and FIB-SEM tomography. Microporous Mesoporous Mater. 208, 1–20.

Honty, M., De Craen, M., Wang, L., Madejová, J., Czímerová, A., Pentrák, M., Strícek, I., Van Geet, M., 2010. The effect of high pH alkaline solutions on the mineral stability of the Boom Clay - batch experiments at 60 °C. Appl. Geochem. 25, 825–840.

Honty, M., Frederickx, L., Wang, L., De Craen, M., Thomas, P., Moors, H., Jacops, E., 2022. Boom Clay pore water geochemistry at the Mol site: Experimental data as determined by in situ sampling of the piezometers. Appl. Geochem. 136.

Hou, L.H., Yu, Z.C., Luo, X., Wu, S.T., 2022. Self-sealing of caprocks during CO₂ geological sequestration. Energy 252.

Jackson, M.L., 1975. Soil Chemical Analysis - Advanced Course, Second, edition ed. Published by the author, Madison, Wisconsin.

Kaufhold, S., Grathoff, G., Halisch, M., Plötze, M., Kus, J., Ufer, K., Dohrmann, R., Ladage, S., Ostertag-Henning, C., 2016. Comparison of methods for the determination of the pore system of a potential GERMAN gas shale. Clay Miner. Soc. Workshop Lectures Series 21, 163–190.

Kuligiewicz, A., Derkowski, A., Szczerba, M., Gionis, V., Chryssikos, G., 2015. Revisiting the infrared spectrum of the water–smectite interface. Clay Clay Miner. 63, 15–29.

Lalan, P., Dauzères, A., De Windt, L., Sammaljärvi, J., Bartier, D., Techer, I., Detilleux, V., Siitari-Kauppi, M., 2019. Mineralogical and microstructural evolution of Portland

cement paste/argillite interfaces at 70 °C – Considerations for diffusion and porosity properties. Cem. Concr. Res. 115, 414–425.
Ma, B., Provis, J.L., Wang, D., Kosakowski, G., 2024. The essential role of cement-based materials in a radioactive waste repository. npj Mater. Sustain. 2, 21.
Madejová, J., 2003. FTIR techniques in clay mineral studies. Vib. Spectrosc. 31, 1–10.
Mäder, U., Jenni, A., Lerouge, C., Gaboreau, S., Miyoshi, S., Kimura, Y., Cloet, V., Fukaya, M., Claret, F., Otake, T., Shibata, M., Lothenbach, B., 2017. 5-year chemico-physical evolution of concrete–claystone interfaces, Mont Terri rock laboratory (Switzerland). Swiss J. Geosci. 110, 307–327.
Martini, M., Francus, P., Trotta, L.D., Després, P., 2021. Identification of Common Minerals using Stoichiometric Calibration Method for Dual-Energy CT. Geochem. Geophys. Geosyst. 22.
Masschaele, B., Dierick, M., Van Loo, D., Boone, M.N., Brabant, L., Pauwels, E., Cnudde, V., Van Hoorebeke, L., 2013. HECTOR: A 240kV micro-CT Setup Optimized for Research, 11th International Conference on X-Ray Microscopy (XRM). Shanghai Synchrotron Radiat Facil, Shanghai, PEOPLES R CHINA.
Mehra, O.P., Jackson, M.L., 1958. Iron oxide removal from soils and clays by a dithionite-citrate system buffered with sodium bicarbonate. In: National Conference on Clays and Clays Minerals, pp. 317–327.
Moore, D., Reynolds, R., 1997. X-Ray Diffraction and the Identification and Analysis of Clay Minerals, 2nd ed. Oxford Univ. Press, New York.
Mystkowski, K., Srodon, J., McCarty, D., 2002. Application of Evolutionary Programming to Automatic XRD Quantitative Analysis of Clay-Bearing Rocks, the Clay Minerals Society 39th Annual Meeting. Boulder, Colorado, Abstracts with Programs.
Nakayama, S., Sakamoto, Y., Yamaguchi, T., Akai, M., Tanaka, T., Sato, T., Iida, Y., 2004. Dissolution of montmorillonite in compacted bentonite by highly alkaline aqueous solutions and diffusivity of hydroxide ions. Appl. Clay Sci. 27, 53–65.
Ramirez, S., Vieillard, P., Bouchet, A., Cassagnabere, A., Meunier, A., Jacquot, E., 2005. Alteration of the Callovo-Oxfordian clay from Meuse-Haute Marne underground laboratory (France) by alkaline solution. I. A XRD and CEC study. Appl. Geochem. 20, 89–99.
Rodriguez-Blanco, J.D., Bots, P., Terrill, N.J., Shaw, S., Benning, L.G., 2010. The mechanism of ACC nanoparticle transformation to vaterite. Geochim. Cosmochim. Acta 74, A876.
Russell, J., Fraser, A., 1994. Infrared methods, clay mineralogy: Spectroscopic and chemical determinative methods. Springer, pp. 11–67.
Seemann, T., Weber, C., Bertier, P., Claes, H., Stanjek, H., 2025. Argon physisorption for pore analysis of mudrocks, clays, and engineered analogues: is argon a better choice than nitrogen and carbon dioxide? Clay Clay Miner. 73.
Sittner, J., Godinho, J.R.A., Renno, A.D., Cnudde, V., Boone, M., De Schryver, T., Van Loo, D., Merkulova, M., Roine, A., Liipo, J., 2021. Spectral X-ray computed micro tomography: 3-dimensional chemical imaging. X-Ray Spectrom. 50, 92–105.
Środoń, J., Drits, V.A., McCarty, D.K., Hsieh, J.C., Eberl, D.D., 2001. Quantitative X-ray diffraction analysis of clay-bearing rocks from random preparations. Clay Clay Miner. 49, 514–528.
Tatzber, M., Stemmer, M., Spiegel, H., Katzlberger, C., Haberhauer, G., Gerzabek, M.H., 2007. An alternative method to measure carbonate in soils by FT-IR spectroscopy. Environ. Chem. Lett. 5, 9–12.
Techer, I., Bartier, D., Boulvais, P., Tinseau, E., Suchorski, K., Cabrera, J., Dauzères, A., 2012. Tracing interactions between natural argillites and hyper-alkaline fluids from engineered cement paste and concrete: Chemical and isotopic monitoring of a 15-years old deep-disposal analogue. Appl. Geochem. 27, 1384–1402.
Tian, H.L., Xu, T.F., Wang, F.G., Patil, V., Sun, Y., Yue, G.F., 2014. A numerical study of mineral alteration and self-sealing efficiency of a caprock for CO₂ geological storage. Acta Geotech. 9, 87–100.
Van Geet, M., Bastiaens, W., Ortiz, L., 2008. Self-sealing capacity of argillaceous rocks: Review of laboratory results obtained from the SELFRAC project. Phys. Chem. Earth 33, S396–S406.
Van Marcke, P., Bastiaens, W., 2010. Excavation induced fractures in a plastic clay formation: Observations at the HADES URF. J. Struct. Geol. 32, 1677–1684.
Vlassenbroeck, J., Dierick, M., Masschaele, B., Cnudde, V., Hoorebeke, L., Jacobs, P., 2007. Software tools for quantification of X-ray microtomography. In: Nuclear Instruments & Methods in Physics Research Section a-Accelerators Spectrometers Detectors and Associated Equipment, 580, pp. 442–445.
Wang, C., Briffaut, M., Talandier, J., Skoczylas, F., 2024. Self-sealing of pre-cracked callovo-oxfordian claystone: Implications for geological disposal of nuclear waste. Int. J. Rock Mech. Min. Sci. 175.
Wang, L., Jacques, D., De Canniere, P., 2010. Effects of an alkaline plume on the Boom Clay as a potential host formation for geological disposal of radioactvie waste. In: External report of SCK-CEN-ER-28, Mol, p. 194.
Wilson, J., Bateman, K., Tachi, Y., 2021. The impact of cement on argillaceous rocks in radioactive waste disposal systems: a review focusing on key processes and remaining issues. Appl. Geochem. 130.
Yu, L., Rogiers, B., Gedeon, M., Marivoet, J., De Craen, M., Mallants, D., 2013. A critical review of laboratory and in-situ hydraulic conductivity measurements for the Boom Clay in Belgium. Appl. Clay Sci. 75-76, 1–12.
Zeelmaekers, E., Honty, M., Derkowski, A., Środoń, J., De Craen, M., Vandenberghe, N., Adriaens, R., Ufer, K., Wouters, L., 2015. Qualitative and quantitative mineralogical composition of the Rupelian Boom Clay in Belgium. Clay Miner. 50, 249–272.
Zhang, C.L., 2011. Experimental evidence for self-sealing of fractures in claystone. Phys. Chem. Earth 36, 1972–1980.
Zhang, C.L., Talandier, J., 2023. Self-sealing of fractures in indurated claystones measured by water and gas flow. J. Rock Mech. Geotech. Eng. 15, 227–238.